Light-induced processes in plasmonic $Gold/TiO_2$ photocatalysts studied by electron paramagnetic resonance

Reference:

Caretti Ignacio, Keulemans Maarten, Verbruggen Sammy, Lenaerts Silvia, Van Doorslaer Sabine.- Light-induced processes in plasmonic $Gold/TiO_2$ photocatalysts studied by electron paramagnetic resonance

Topics in catalysis - ISSN 1022-5528 - 58:12(2015), p. 776-782

Full text (Publishers DOI): http://dx.doi.org/doi:10.1007/s11244-015-0419-4

Light-Induced Processes in Plasmonic Gold/TiO_2 Photocatalysts Studied by Electron Paramagnetic Resonance

Ignacio Caretti [1]

Maarten Keulemans [2,3]

Sammy W. Verbruggen [2,3]

Silvia Lenaerts [2]

Sabine Van Doorslaer [1,*]

Phone +32/3/2652461
Email sabine.vandoorslaer@uantwerpen.be

[1] BIMEF, Department of Physics, University of Antwerp, Universiteitsplein 1, 2610 Antwerp, Belgium

[2] Sustainable Energy and Air Purification, Department of Bioscience Engineering, University of Antwerp, Groenenborgerlaan 171, 2020 Antwerp, Belgium

[3] Department of Microbial and Molecular Systems, Center for Surface Chemistry and Catalysis, KU Leuven, Kasteelpark Arenberg 23, 3001 Heverlee (Leuven), Belgium

Abstract

X-band and W-band continuous-wave (CW) electron paramagnetic resonance (EPR) was used to study in situ light-induced (LI) mechanisms in commercial P90 titania (90 % anatase/10 % rutile) compared to plasmon-enhanced Au-P90 photocatalyst. These materials were excited using UV and 532 nm visible light to generate different excitation states and distinguish pure charge separation from plasmon-assisted resonance processes. Up to nine different photoinduced species of trapped electrons and holes were identified. LI CW EPR of P90 is

presented for the first time, showing a UV excitation response similar to the well-known mixed-phase P25 titania. It is shown that incorporation of Au nanoparticles in Au-P90 and formation of a Schottky junction affects the charge separation state of the catalyst under UV light. Moreover, Au impregnation activated P90 through plasmon 'hot' electron injection under visible light excitation ("plasmonic sensitization effect"). In general, EPR proved to be crucial to determine the different photoexciation paths and reactions that regulate plasmonic photocatalysis.

Keywords

EPR
Photocatalysis
Titanium dioxide
Plasmon
Gold

Electronic supplementary material

The online version of this article (doi:10.1007/s11244-015-0419-4) contains supplementary material, which is available to authorized users.

1. Introduction

Titanium dioxide photocatalysts are promising materials for water and air purification and artificial photosynthesis [1–3]. One of the key steps in the photocatalytic process involves the light-induced excitation of an electron from the valence to the conduction band. The wide bandgap (3.0–3.2 eV) of most titanium dioxide materials implies the use of UV light (<380 nm) for this activation step, which restricts the applicability of these materials. Therefore, a lot of effort has been devoted to the synthesis of TiO_2-based materials that enable the use of visible-light wavelengths as well [4]. These efforts include doping of titanium dioxides [5, 6], synthesis of TiO_2-based mesoporous materials or nanoparticles [7], coupling with other semi-conductors [4], incorporation of carbonaceous nanomaterials [4, 8], and modification of titanium dioxide with noble metal nanoparticles [9]. In the latter case this is achieved by exploiting the surface plasmon resonance (SPR) effect.

In order to modify the properties of titanium dioxide-containing materials, an in-depth insight in the photocatalytic process is vital. A large number of paramagnetic centres can result from the initial photo-generated electron–hole pair [10]. Trapping of valence band holes by O^{2-} can for instance lead to O^{-} that can form O_3^{-} after combination with dioxygen. Conduction band electrons can be trapped by Ti^{4+} ions resulting in Ti^{3+}. On the surface, these Ti^{3+} ions can then react with dioxygen to form O_2^{-}. Electron paramagnetic resonance (EPR) has been shown to be a prime technique to detect these light-induced paramagnetic species and thus unravel the different mechanistic steps involved in the photocatalysis of titanium dioxide materials [10].

Recently, some of us have shown that deposition of gold-silver alloy nanoparticles on P90 titanium-dioxide materials provides a powerful strategy to boost the visible light response of the photocatalyst [11]. By tuning the value of x in the $Au_xAg_{(1-x)}$ nanoparticles, the plasmon resonance frequency can be shifted over a broad range of visible light wavelengths [12], which helped to tune the photocatalytic response. The plasmonic photocatalyst formed by $Au_{0.3}Ag_{0.7}$ nanoparticles on P90 titanium dioxide proved to be significantly more efficient toward stearic acid degradation under illumination at 490 nm than the pristine titanium dioxide. In the current work, we used EPR to unravel the light-induced species formed in plasmonic photocatalysts for the case of pure gold modified P90 titania. A considerable number of studies on Au-deposited TiO_2 particles and films have clearly shown a plasmon-enhanced photocatalytic activity of TiO_2 under visible-light irradiation [13]. Whether this activation occurs through transfer of plasmon-excited ‘hot’ electrons from the metal to the catalyst or via strong local near field effects is still a matter of debate [14]. For this reason, the effect of UV and visible-light illumination on the photo-induced paramagnetic centres in both the pristine and plasmonic photocatalyst is compared. In order to disentangle the different contributions to the EPR spectrum, EPR experiments were performed at standard (X-band, ~9.5 GHz) and high (W-band, ~95 GHz) microwave frequencies. Although it has been extensively demonstrated that high-frequency (or high-field) EPR provides enhanced spectral resolution [15], W-band light-induced EPR has only scarcely been applied to the study of TiO_2-based materials [16, 17]. Furthermore, although a recent review on TiO_2 modified with noble metals recognizes

the importance of EPR as a unique tool to understand the superior photocatalytic activity of these materials [9], only few EPR studies have been reported on the topic [18–23].

2. Experimental

2.1. Plasmonic Photocatalyst Synthesis

The synthesis of the plasmonic photocatalysts is detailed in [11]. In short, a commercially available TiO_2 source, P90 (Evonik, 90 % anatase, 10 % rutile with mean crystallite size 14 nm and specific surface area 90 ± 20 $m^2\ g^{-1}$) was used. $HAuCl_4.3H_2O$ (both Sigma-Aldrich, >99.9 %) was used for the synthesis of the colloidal Au nanoparticles following a modified Turkevich synthesis strategy. Two photocatalysts are studied here by EPR: (i) pristine P90 and (ii) Au nanoparticles on P90 (Au-P90). While pristine P90 absorbs light below 400 nm, Au-modified P90 samples show a plasmon absorption band in the visible light (see Supplementary Information). The maximum SPR absorption band is found at 542 nm for Au on P90. XRD patterns, BET surface areas and FTIR spectra before and after Au impregnation show no major structural change in P90 as a result of the synthesis method (see Supplementary Information). Moreover, FTIR indicates hydration of both P90 and Au-P90 surfaces and the introduction of C contamination through the use of sodium citrate as reducing agent during the synthesis and impregnation procedures (Figures S3-S5).

2.2. EPR Spectroscopy

All X-band continuous wave (CW) EPR experiments were performed under air on a Bruker ESP300E spectrometer (microwave (mw) frequency ~9.44 GHz) equipped with a liquid Helium cryostat (Oxford Inc.). The EPR spectra were taken with a modulation amplitude of 0.2 mT and a modulation frequency of 100 kHz. The microwave power was 0.5 mW. The temperatures at which the spectra were recorded are given in the figure captions. The samples were either irradiated with UV light (a deuterium lamp at 1.5 A with a 220 nm broadband interference filter) or visible light (532 nm of a frequency-doubled, diode-pumped Nd:YAG laser).

All W-band EPR experiments were performed on a Bruker Elexsys E680 spectrometer equipped with a continuous gas flow crysostat from Oxford instruments. The sample was not evacuated prior to insertion in the cavity.

CW-EPR experiments were performed with a modulation amplitude of either 0.4 or 1 mT and a modulation frequency of 100 kHz. The microwave power was 0.022 mW. *In situ* UV illumination was done using the 350.7 nm laser line of Kr^+ ion laser (Spectra Physics 2580). Visible light illumination was done as in the X-band set-up.

No EPR signals were observed in the photocatalysts without illumination. All EPR spectra have been normalized and simulated using the EasySpin, a MATLAB toolbox developed for EPR simulations [24]. The relative ratio of the EPR contributions used to simulate all the spectra can be found in Table S1 of the Supplementary Information.

3. Results and Discussion

3.1. UV Light

Figure 1 shows the experimental (a, b) and simulated (a′, b′) X-band CW-EPR spectra of pristine P90 and Au-P90 after 90 min illumination with UV light. Before illumination no EPR signal was detected. The EPR spectra of the individual species contributing to each simulation are also displayed and labelled with roman numerals. A summary of their ***g***-tensor parameters is presented in Table 1, while their relative ratio in the simulations can be found in the Supplementary Information (Table S1). It is clear from Fig. 1 that P90 and Au-P90 exhibit a completely different light-induced (LI) EPR signal under UV-light excitation, already suggesting a different photoresponse due to the presence of gold nanoparticles.

Fig. 1

Normalized experimental X-band CW-EPR of P90 (**a**) and Au-P90 (**b**) recorded after 90 min UV illumination at 10 K. The corresponding simulated spectra (a′, b′) and the individual contributions of species I-VIII used in the simulation are also shown. See Table 1 for corresponding *g* parameters

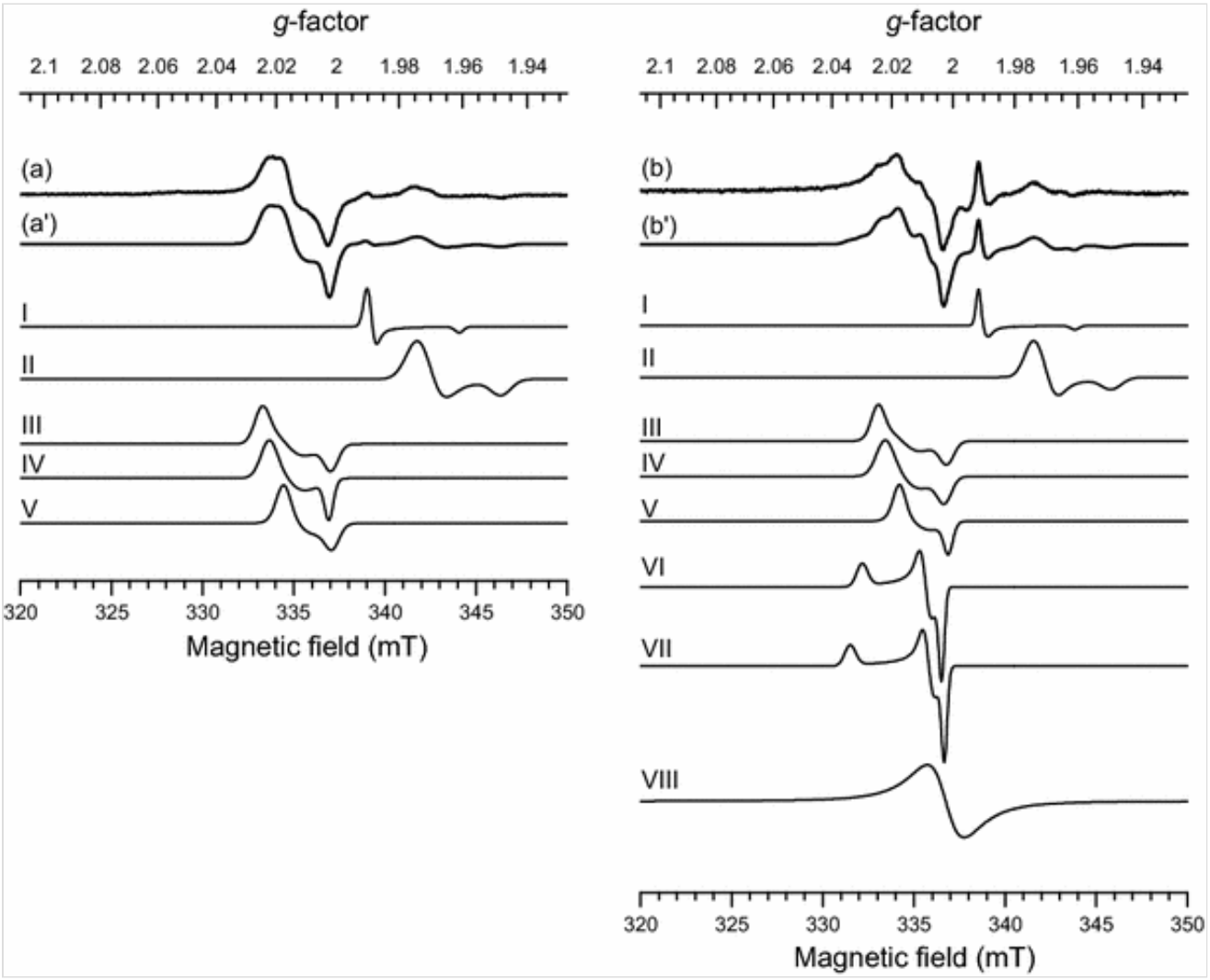

Table 1

Summary of the ***g*** tensor values of all the species detected under UV and visible light in the systems under study.

	Assignment	g_x	g_y	g_z
Species I	Ti^{3+} in anatase	1.9900	1.9900	1.961
Species II	Ti^{3+} in rutile	1.9747	1.9695	1.9495
Species III	O^-	2.0243	2.0162	2.0021
Species IV	O^-	2.0221	2.0159	2.0030
Species V	O_3^-	2.0170	2.0123	2.0018
Species VI	$HO_2^{\bullet}$	2.0037	2.009	2.030
Species VII	$HO_2^{\bullet}$	2.0028	2.008	2.034
Species VIII	Conduction electrons		2.0023	
Species IX	C-centered radical	2.0038	2.0036	2.0014
Experimental error is on the last digit given				

The EPR signal (a) of the P90 support is typical of TiO_2 materials, where oxygen-radical related ($g > 2$) and Ti^{3+} ($g < 2$) paramagnetic species are observed. Species I and II are well-known in titania and correspond to bulk Ti^{3+} centers in anatase and rutile, respectively, formed by reduction of lattice Ti^{4+} by photoexcited electrons [16, 25]. As also reported for Degussa P25 under UV illumination [26, 27], a relative larger contribution (See Table S1) of bulk Ti^{3+} sites from rutile compared to anatase is observed in the CW-EPR spectrum of P90, which indicates a higher electron trapping at the less abundant (10 %) rutile phase than at the preponderant (90 %) anatase phase. Hence, the same mechanism of electron transfer at the rutile-anatase interface of P25 [26] can be used here to explain the photoinduced charge separation in P90. The g values of species III and IV are very similar and are characteristic of bulk O^- rhombic centres from holes trapped at lattice O^{2-} sites [25, 28]. These centres cannot be mistaken with O_2^- superoxide anions in different environments, since the latter have always g_y values of approximately 2.008-2.01 producing a more rhombic EPR spectrum than for O_2^- [29, 30]. The presence of two O^- species suggests two slightly different trapping sites at the anatase and/or rutile phases of P90. Based on the fact that the experiments are carried out under air and on the g values obtained, species V can be attributed to O_3^- after reaction of molecular oxygen with surface O^- species [31]. The g values of O_3^- centres depend only slightly on the matrix [31]. The large content of molecular oxygen in air will significantly enhance paramagnetic relaxation, what may explain here the quenching of O_2^- superoxide signals that are commonly detected in TiO_2 materials by EPR. Observation of O_2^- radicals is indeed often achieved by exposing the reduced sample to controlled O_2 atmospheres at low pressures (10–50 mbar) before acquisition [30, 32] or by irradiation in O_2 during the measurement [14, 30]. Moreover, the hydrated state of the catalyst surface (Figure S3) can also lead to the transformation of O_2^- radicals into H_2O_2 diamagnetic species [30], hindering its detection. For a correct determination of the number of oxygen species present and their g parameters it was necessary to resort to W-band EPR experiments, since species III-V considerably overlap in the LI CW-EPR spectrum at X-band with a substantial broadening caused by paramagnetic relaxation.

The experimental (a) and simulated (a′) W-band CW-EPR spectra of P90

after UV excitation for 170 min are displayed in Fig. 2, together with the individual species I-V used for its simulation. An additional contribution of Mn^{2+} from the cavity also needed to be added. To improve the signal-to-noise ratio the region corresponding to Ti^{3+}-related species (a″) was recorded after accumulation of 8 scans over 1 h of continuous UV illumination, following 3 h of prior UV excitation. In this way, all *g* parameters could be determined with high precision and used for the simulation of the X-band spectrum, which confirmed the afore-mentioned assignments for species I-V.

Fig. 2

W-band CW-EPR experimental (*a*) and simulated (*a*′) spectrum of pristine P90 recorded at 16 K under UV 350.7 nm laser light excitation from a Kr laser. The individual EPR spectra of the five species used for the simulation are also depicted plus a Mn^{2+} cavity background signal. The region of the EPR spectrum attributed to Ti^{3+} species could be recorded in detail after more than 3 h UV illumination (spectrum (*a*″))

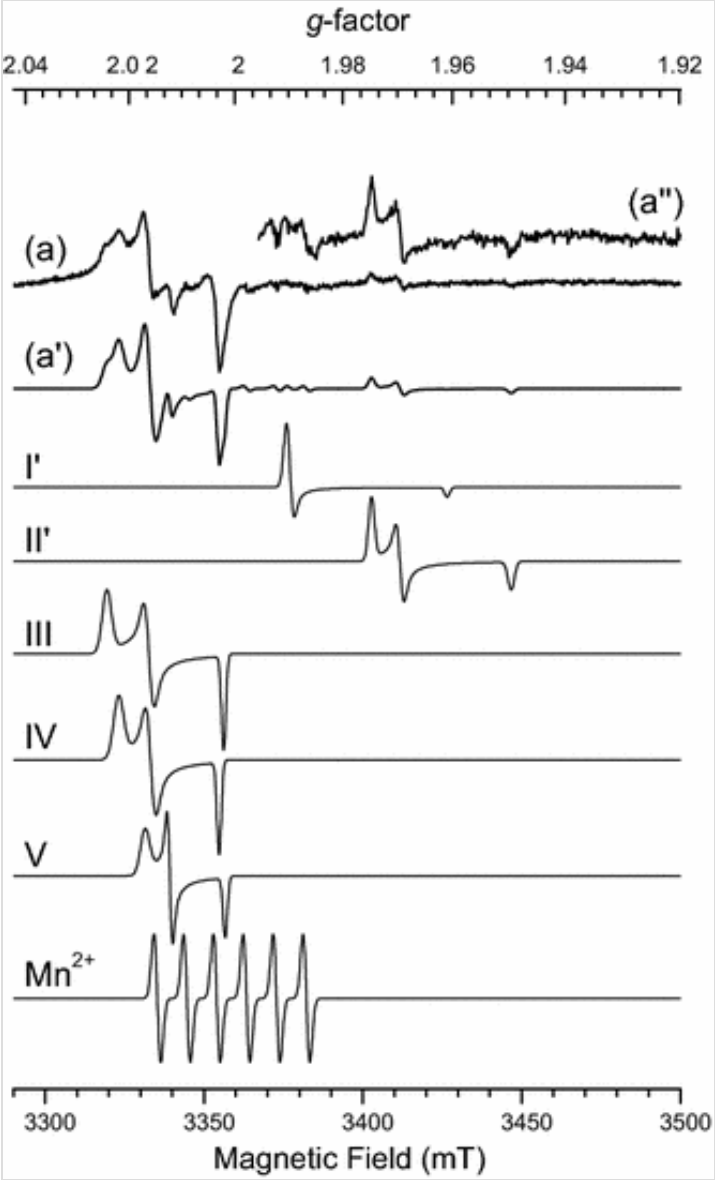

The above demonstrates that under UV-light irradiation P90 titania undergoes the expected charge separation and generation of EPR-detectable electron and hole carriers, similar to the case of P25. Electrons are detected after trapping in the form of Ti^{3+} centres in both the rutile and anatase phase. The low intensity of these Ti^{3+} species and the fact that they are generated in the bulk of P90 nanoparticles, indicates a fast recombination and trapping process of photo-generated electrons before they can reach the catalyst surface. On the other hand, the detection of O_3^- shows the interaction of hole-induced O^- species at the surface of P90 with environmental dioxygen. As previously mentioned, detection of the commonly observed O_2^- species may be shunned by paramagnetic relaxation effects under air or by reaction with surface hydroxyl groups and formation of EPR-silent hydrogen peroxide.

In the case of the Au-P90 nanocomposite, the situation is different. When

the Au metal nanoparticle and the P90 semiconductor are brought together a Schottky junction is formed under good electrical contact [9, 33]. In that situation, a space charge region is formed at the metal semiconductor interface that facilitates charge separation under UV illumination and will counteract charge carrier recombination. The benefits of a Schottky-barrier formation and charge transfer in Au-TiO_2 systems have been widely used to increase the photocatalytic performance of pristine titania [33]. Even though Au can absorb UV light, the photon energy is too high to generate a surface plasmon in Au, and the metal acts mainly as a scavenger of conduction band electrons from the semiconductor. However, it has been recently suggested that the electrons promoted from the 5d band to the 6sp conduction band in Au under UV excitation have sufficient energy to interact with the environment at the metal surface, increasing the number of active carriers and the catalytic performance [9]. This mechanism has been proposed to be responsible for the degradation of sulforhodamine-B under UV illumination of gold nanoparticles in different supports that hardly absorbed any UV light at the used wavelength [34].

CW-EPR spectra (a) and (b) in Fig. 1 reveal a remarkable increase of the relative ratio of anatase to rutile Ti^{3+} centres (i.e. species I to species II) under UV illumination for Au-P90 compared to P90 alone. The same species III-V discussed above also contribute to the EPR spectrum (b) but in different relative amounts (See Table S1). The appearance of a new EPR signal at $g \sim 2.03$ and a distinct peak at $g \sim 2.01$ led to the identification of species VI and VII. The g parameters of species VI and VII are consistent with the formation of O_2^- radicals by reaction of photogenerated electrons with molecular oxygen at the P90 and/or metal surface. However, the g_z values reported for O_2^- radicals in titania are commonly lower than 2.03 [29, 30, 32], pointing to a different nature of species VI and VII. Notice that a g_z value of approximately 2.034 is considered a clear fingerprint for peroxy radical formation. Indeed, in case O_2^- radicals further react with surface hydroxyl groups they form hydroperoxy radicals ($HO_2^\bullet$), whose characteristic g values coincide with the ones of species VI and VII [30, 32]. Since $HO_2^\bullet$ species are not observed in pristine P90 we attribute their presence to a gold-related excitation path. As mentioned above, UV light is enough to excite electrons within the metal that interact at the surface with air to form O_2^- radicals, which further react with hydroxyl groups at the P90 surface to give $HO_2^\bullet$. In agreement with this, the hydrated state of the P90 surface has been clearly assessed by FTIR (Figure S4). These results

suggest a partial hydration of the catalyst surface, since a fully hydrated surface has been reported to completely quench the EPR signals [30]. Finally, the addition of a 3.5mT broad Gaussian line (labelled species VIII) is needed to properly simulate the whole EPR line shape. The latter can be assigned to conduction electrons in the Au nanoparticles. Conduction electrons in metallic nanoparticles often give rise to EPR signals of this kind with linewidths that vary from a few to tenths of mT depending mainly on their size and type of metal [35].

The UV-induced EPR experiments on Au-P90 reveal also a difference in the relative ratio of species from both photogenerated electrons and holes in comparison to the P90 case (See Supplementary Information). Moreover, new $HO_2^{\bullet}$ surface species are detected, and a gold-based excitation mechanism is proposed. Notice that for P90 bulk species I–IV and surface species V–VIII represent 29.9 and 70.1 % of the EPR spectrum, respectively, whereas these values are 27.4 and 72.6 % for Au-P90 (See Table S1). The population of the conduction band states of the Au nanoparticles (species VIII) has been considered as bulk species arising from the transfer of electron carriers from P90 to the gold nanoparticles, and possibly also Au interband excitation. These results indicate that the relative ratio of surface to bulk species is similar in both P90 and Au-P90, being uncertain in our case the beneficial role of a schottky junction in the charge separation process. However, new excitation paths are created by the presence of gold itself as electron sink, giving rise to new surface species.

3.2. Visible Light

The X-band CW LI-EPR spectra of pristine P90 and Au-P90 catalysts have been recorded under excitation with green laser light of 532 nm. The experimental (a, b) and simulated (b′) spectra are shown in Fig. 3, as well as the individual species I, II and IX used for the simulations (see Table 1 for *g* parameters). UV–vis spectroscopy shows that the use of 532 nm light will efficiently excite a surface plasmon in Au-P90, but will not be absorbed by the P90 titania particles [11]. In this way we can elucidate whether creation of a surface plasmon state can be utilized to activate the visible-light response of P90. To the best of our knowledge, an EPR study on visible-light plasmonic activation of P90 titania has not yet been reported.

Fig. 3

X-band CW-EPR spectra of (*a*) P90 and (*b*) Au-P90 after illumination with 532 nm laser light for 90 min at 10 K. Species *I*, *II* and *IX* used for the simulation (*b*′) are also shown

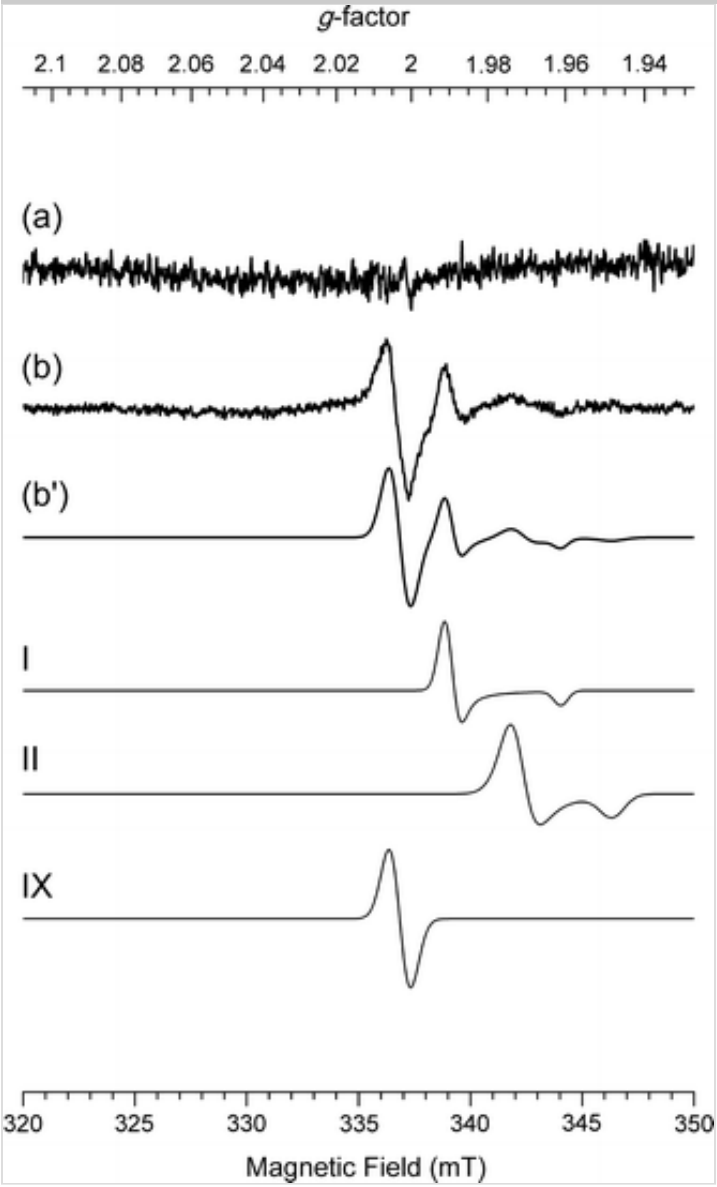

No photo-induced charge separation is achieved by visible-light excitation of pristine P90 (Fig. 3a). Thus, the P90 catalyst is not activated at this wavelength, in line with the poor degradation of stearic acid reported for this same material under 490 nm illumination [11]. On the contrary, spectrum 3(b) from the Au-P90 nanocomposite shows clear EPR intensity under visible light excitation. The species I and II also detected for UV-illuminated Au-P90 (Fig. 2b) are observed here. This shows the trapping of electrons by Ti^{4+} sites in rutile and anatase with the formation of Ti^{3+} in the bulk of P90. In addition, a new signal (species IX) shows up at

g_{iso} ~ 2.003 with a peak to peak linewidth of 1.1mT that is commonly assigned to F^+-colour centres, *i.e.* an electron trapped in an oxygen vacancy [16, 31]. However, Fig. 4 shows the corresponding W-band EPR signal of Au-P90 obtained after excitation with 532 nm laser light and a clear rhombicity of the ***g*** tensor is resolved (see Table 1). Since this anisotropy of the ***g*** tensor is surprising for F^+ centres (highly isotropic), it is likely that this EPR signal arises from a carbon-centred radical. Very similar *g* values have for instance been reported for CO_3^{3-} [36]. In fact, a number of intermediate carbon-centered radicals including CO_3^{2-} have been identified in the photoreduction process of CO_2 by titania [37]. EPR signals similar to species IX have been found also in C-doped TiO_2 materials [16] and for Au/Pd nanoparticles on TiO_2 under visible light [22]. Unlike in this work, the latter EPR study did not reveal Ti^{3+} species probably because the experiments were carried out at too high temperature (90 K) to allow a good detection of these species. Furthermore, FTIR spectra of unmodified P90 (subjected to the same impregnation procedure; Figure S5) and the Au-modified P90 (Figure S4) confirm the presence of vibration modes from carbon-based species (C=O, CH_2 and CH_3; Table S3), likely due to the use of sodium citrate as reducing agent. The microwave power dependence of species IX in Au-P90 (Figure S6) shows no intensity saturation at powers as high as 20 mW under 532 nm illumination at room temperature. This result is incompatible with an isolated defect like F^+ centers, with relatively long relaxation times.

Fig. 4

W-band CW-EPR spectrum of the Au-P90 nanocomposite recorded after 150 min illumination with 532 nm laser light at 10 K

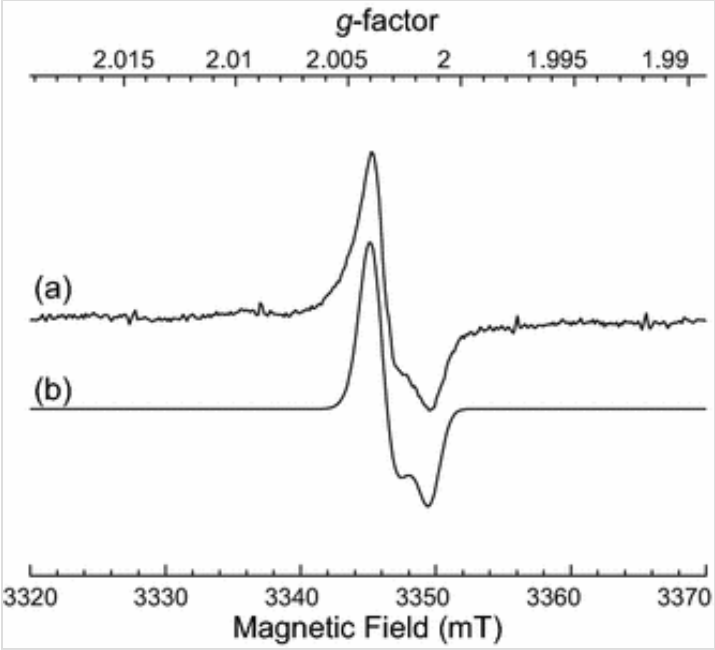

The above discussed results demonstrate the plasmon-induced visible light activation of P90 by deposition of Au nanoparticles, whose peak plasmon resonance is 542 nm. The observation of bulk Ti^{3+} paramagnetic centres formed by electron trapping are a definite proof of this. Interestingly, only electron-induced signals are observed in the LI-EPR spectra of the Au-P90 nanocomposite, and no hole-related signals are detected, unlike in the case of UV-light illumination. In general, two mechanisms can be considered here for the plasmonic enhancement of metal/P90 photocatalysts compared to pristine P90: surface plasmon sensitization and strong near-field effects [9]. The latter mechanism is a consequence of plasmon resonance energy transfer to the semiconductor caused by strong localized electric fields in the vicinity of the metallic nanoparticle, with the subsequent formation of electron–hole pairs. Given that no hole-related species have been detected we are inclined to discard this mechanism as the main activation process of P90 under visible light. Furthermore, the near-field enhancement effect requires an overlap of the plasmon band and semiconductor bandgap energies, which is clearly not the case. Instead, plasmon sensitization consists in the generation of a plasmon resonance in the metallic nanoparticle and “hot” electrons through non-radiative decay, which then acquire enough energy to overcome the Schottky barrier and can be transferred to the P90 semiconductor. The EPR results suggest that this is the main mechanism of P90 activation in the Au-P90 photocatalyst under visible light. This means that the detection of trapped electrons in P90 by EPR is due to the injection of electrons into the P90 conduction band after surface plasmon resonance, in agreement with previous work of Au

supported P25 with smaller Au nanoparticles (<5 nm) [38, 39] or of similar diameter [14]. Interestingly, our results are in contradiction with those recently reported on an Au-modified P25 with similar particle size, where near fields were proposed as main promoting effect in the oxidation of methylcyclohexane at 425 nm whilst no catalytic activity was found at a wavelength of 525 nm [40]. The authors based the assigned mechanism on a too short electron mean free path to allow electron injection and the predominance of field effects when there is some absorption overlap between Au and P25. However, in our study, the Au nanoparticles are smaller than the electron mean free path of gold (~50 nm), and there is no absorption overlap at 532 nm excitation. Finally, note that localized heating effects due to metal temperature increase through electron–phonon relaxation are not detectable by EPR, and plasmon-enhanced light scattering effects can be discarded because P90 does not absorb green light.

4. Conclusion

The light-induced processes that govern plasmonic Au-P90 photocatalysis have been elucidated by X-band and W-band EPR and compared to the pristine P90 catalyst. Illumination with UV and visible (532 nm) light allowed the creation of dual-excitation and surface plasmon resonance states, respectively. In this way, participation of P90 and the metallic particles in the light activation routes could be disentangled. The LI X-band CW EPR of P90 has been measured for the first time, showing a behaviour comparable to the well-known P25 titania. Under UV-light both P90 and the Au particles are excited and EPR showed a comparable amount of relative surface to bulk species. This does not point to a better charge separation in the TiO_2 catalyst due to a Schottky junction, but to a redistribution of charge carriers due to the presence of Au as electron scavenger and formation of new surface species. When green light is used as excitation source, P90 is EPR silent while Au-P90 exhibits an EPR signal, which is a definitive proof of titania visible-light activation through plasmon resonance. All the EPR signals detected under visible light are related to trapped electrons in P90, which in turn, points to plasmon resonance sensitization as the predominant mechanism of P90 visible-light activation.

Acknowledgments

IC and SVD acknowledge the Research Foundation—Flanders (FWO) for financial support (Grant G.0687.13). SV thanks FWO for financial support through a postdoctoral fellowship and MK acknowledges the agency for Innovation by Science and Technology in Flanders (IWT) for financial support (Ph.D. Grant).

5. Electronic supplementary material

Below is the link to the electronic supplementary material.

Supplementary material 1 (PDF 478 kb)

References

1. Anpo M, Kamat PV (eds) (2010) Environmentally benign photocatalysts: Applications of titanium oxide-based materials. Springer, New York

2. Thompson TL, Yates JT (2006) Chem Rev 106:4428–4453

3. Pichat P (ed) (2013) Photocatalysis and water purification: from fundamentals to recent applications. Wiley-VCH, Weinheim

4. Dahl M, Liu Y, Yin Y (2014) Chem Rev 114:9853–9889

5. Akpan UG, Hameed BH (2010) Appl Catal A 375:1–11

6. Pelaez M, Nolan NT, Pillai SC, Seery MK, Falaras P, Kontos AG, Dunlop PSM, Hamilton JWJ, Byrne JA, O'Shea K, Entezari MH, Dionysiou DD (2012) Appl Catal B 125:331–349

7. Vivero-Escoto JL, Chiang Y-D, Wu KC-W, Yamauchi Y (2012) Sci Technol. Adv Mater 13:013003

8. Ong W-J, Gui MM, Chai S-P, Mohamed AR (2013) RSC Adv 3:4505–4509

9. Bumajdad A, Madkour V (2014) Phys Chem Chem Phys 16:7146–7158

10. Kumar SG, Devi LG (2011) J Phys Chem A 115:13211–13241

11. Verbruggen SW, Keulemans M, Filippousi M, Flahaut D, Van Tendeloo G, Lacombe S, Martens JA, Lenaerts S (2014) Appl Catal B 156–157:116–121

12. Verbruggen SW, Keulemans M, Martens JA, Lenaerts S (2013) J Phys Chem C 117:19142–19145

13. Zhang X, Chen YL, Liu RS, Ping DP (2013) Rep Prog Phys 76:046401

14. Priebe JB, Karnahl M, Junge H, Beller M, Hollmann D, Brückner A (2013) Angew Chem Int Ed 52:11420–11424

15. Möbius K, Savitsky A (2009) High-field EPR spectroscopy on proteins and their model systems. RSC Publishing, Cambridge

16. Fittipaldi M, Gatteschi D, Fornasiero P (2013) Catal Today 206:2–11

17. Fittipaldi M, Gombac V, Montini T, Fornasiero P, Graziani M (2008) Inorg Chim Acta 361:3980–3987

18. Vijayan BK, Dimitrijevic NM, Wu J, Gray KA (2010) J Phys Chem C 114:21262–21269

19. Naldoni A, D'Arienzo M, Altomare M, Marelli M, Scotti R, Morazzoni F, Selli E, Dal Santo V (2013) Appl Catal B 130–131:239–248

20. Kubacka A, Ferrer M, Martínez-Arias A, Fernández-García M (2008) Appl Catal B 84:87–93

21. Zhang N, Liu S, Fu X, Xu Y-J (2011) J Phys Chem C 115:9136–9145

22. Cybula A, Priebe JB, Pohl MM, Sobaczak JW, Schneider M, Zielinska-Jurek A, Brückner A, Zaleska A (2014) Appl Catal B 152–

153:202–211

23. Liu SX, Qu ZP, Han XW, Sun CL (2004) Catal Today 93–95:877–884

24. Stoll S, Schweiger A (2006) J Magn Reson 178:42–55

25. Chiesa M, Paganini MC, Livraghi S, Giamello E (2013) Phys Chem Chem Phys 15:9435–9447

26. Hurum DC, Agrios AG, Gray KA, Rajh T, Thurnauer MC (2003) J Phys Chem B 107:4545–4549

27. Smits M, Ling Y, Lenaerts S, Van Doorslaer S (2012) Chem Phys Chem 13:4251–4257

28. Micic OI, Zhang Y, Cromack KR, Trifunac AD, Thurnauer MC (1993) J Phys Chem 97:7277–7283

29. Carter E, Carley AF, Murphy DM (2007) J Phys Chem C 111:10630–10638

30. Attwood AL, Murphy DM, Edwards JL, Egerton TA, Harrison RW (2003) Res Chem Intermed 29:449–465

31. Ribbens S, Caretti I, Beyers E, Zamani S, Vinck E, Van Doorslaer A, Cool P (2011) J Phys Chem C 115:2302–2313

32. Carter E, Carley AF, Murphy DM (2007) Chem Phys Chem 8:113–123

33. Zhang X, Chen YL, Liu R, Tsai DP (2013) Rep Prog Phys 76:046401

34. Zhu H, Chen X, Zheng Z, Ke X, Jaatinen E, Zhao J, Guo C, Xie T, Wang D (2009) Chem Commun 48:7524–7526

35. Claus P, Brückner A, Mohr C, Hofmeister H (2000) J Am Chem Soc 122:11430–11439

36. Sadlo J, Matthys P, Vanhaelewyn G, Callens F, Michalika J, Stachowicza W (1998) J Chem Soc Faraday Trans 94:3275–3278

37. Liu L, Li Y (2014) Aerosol Air Qual Res 14:453–469

38. Tsukamoto D, Shiraishi Y, Sugano Y, Ichikawa S, Tanaka S, Hirai T (2012) J Am Chem Soc 134:6309–6315

39. Gomes Silva C, Juárez R, Marino T, Molinari R, García H (2011) J Am Chem Soc 133:595–602

40. Amrollahi R, Hamdy MS, Mul G (2014) J Catal 319:194–199